
Supporting Information for:
A Coarse-Grained Model of Unstructured Single-Stranded DNA Derived from
Atomistic Simulation and Single-Molecule Experiment

Christopher Maffeo, Thuy T. M. Ngo, Taekjip Ha, and Aleksei Aksimentiev

All-atom simulations of ssDNA

Initial parameterization of our CG model was based on the all-atom simulations of a dT₆₀ molecule in a 80×80×80 Å³ volume of 100 or 1000 mM NaCl electrolyte solutions. The reported molarity was determined by counting the total number of chloride ions and water molecules in the system, not taking into account 59 cations added to neutralize the charge of the DNA strand. An ensemble of 21 simulations was performed for both 100 and 1000 mM systems, providing an aggregate simulation time of 6.2 and 3.4 μs, respectively. The initial conformations for the ensemble simulations were randomly chosen from a 1.3-μs trajectory of a dC₆₀ molecule; the cytosine bases were mutated into thymines using the psfgen package. We chose not to present a CG model derived from the all-atom simulations of dC₆₀ because of the following possible artifact of the all-atom model. For poly(dC), we observed hydrogen bonds formed by the amine groups of the cytosine bases and the phosphate groups of the neighboring nucleotides about 5% of the time. We have recently found that the CHARMM amine-phosphate interaction is overestimated. Such persistent hydrogen bonding promoted relatively closed P_n-P_{n+1}-P_{n+2} angles (peak around 120°), which was not observed in dT.

Our all-atom MD simulations were performed using the program NAMD,¹ the CHARMM36 force field,²⁻⁵ the TIP3P model of water,⁶ and standard parameters for ions⁷ with NBFIX corrections applied to ion-nucleic acid interactions.⁸ Van der Waals energies and short-range electrostatics were calculated using a smooth (7–8 Å) cutoff. Periodic boundary conditions were employed and long-range electrostatics were calculated using the particle-mesh Ewald⁹ (PME) method over a 1.2 Å per grid PME array. Integration was performed using 2–2–6 fs multiple timestepping.¹⁰ To enable 2-fs timestepping for bonded interactions, water bonds (and angles) and non-water covalent bonds with hydrogens were held rigid using the SETTLE¹¹ and RATTLE¹² algorithms, respectively. Steric clashes that were introduced during the assembly of the systems were removed through minimization using a conjugate gradient method. Subsequent simulations were performed in the NPT en-

semble. A temperature of 291 K was maintained by applying Langevin forces¹³ to all non-hydrogen atoms (1 ps⁻¹ damping coefficient). A pressure of 1 bar was maintained by Nosé-Hoover Langevin piston pressure control.¹⁴

CG simulations of ssDNA

All CG simulations of our model were carried out using a custom version of the MD program NAMD.¹ The custom version of the code allowed for tabulated potentials to be used to describe bond, angle, and dihedral interactions (resolutions of 0.02 Å, 1°, and 2°, respectively). Piecewise cubic (Catmull-Rom) interpolation was used to calculate the forces due to such potentials at each timestep. Non-bonded interactions were calculated using tabulated non-bonded potentials and a smooth (34–35 Å) cutoff. Stochastic forces from the solvent were mimicked via a Langevin thermostat set to a temperature of 291 K and a damping coefficient of 1.24 ps⁻¹. The mass of each CG bead was set to the mass of the atoms it was designed to represent (the mapping procedure is described in the main text): 160.1 and 181.1 Da for the P and B beads, respectively. Integration was performed using a 20-fs timestep.

Bonded interactions and potentials

Figure S1A-C shows the distributions of the distances between P and B beads within the same nucleotide (P_n-B_n), adjacent P beads (P_n-P_{n+1}), and the B and P beads of adjacent nucleotides (B_n-P_{n+1}). The subscript refers to the nucleotide number that increases in the 5'-to-3' direction, see Figure 1 of the main text. The distributions obtained from the all-atom and CG models are in perfect agreement. The distributions are characterized by narrow (~1 Å width) peaks and a small skew. The distributions of the P_n-B_n and B_n-P_{n+1} bonds differ significantly, suggesting that a structurally precise CG model must apply different potentials to describe these bonds. In particular, the B_n bead is found, on average, closer to the P_n bead than to the P_{n+1} bead; the P_n-B_n distribution has broader peaks than the P_{n+1}-B_n one. By preserving the asymmetry of P_n-B_n and P_{n+1}-B_n bonds, the 5'-to-3' directionality of the DNA strand is incorporated

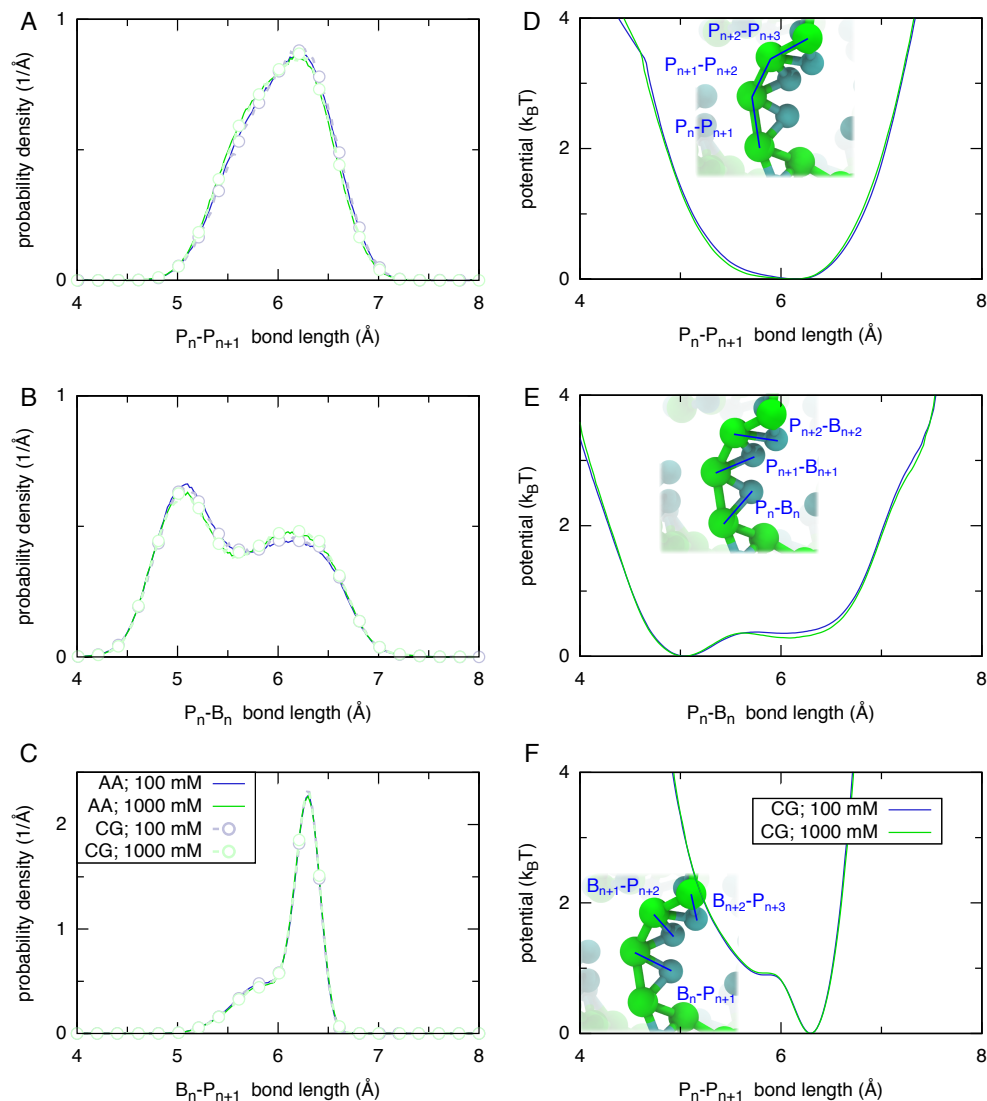


Figure S1: Parameterization of bonded interactions. (A-C) Distributions of bond lengths in all-atom and coarse-grained simulations of a dT₆₀ molecule at 0.02 Å resolution. The solid lines depict the distributions obtained from all-atom simulations in 100 (blue) and 1000 (green) mM NaCl electrolytes. The open circles connected by dashed lines depict the distributions obtained from CG simulations at the 100 (light-blue) and 1000 (light-green) mM conditions. (D-F) The final CG bond length potentials corresponding to the 100 (blue) and 1000 (green) mM conditions. The inset of each panel highlights three bonds of the type characterized in that row of the figure. The image shows a CG representation of ssDNA molecule oriented to have its 5'-to-3' direction pointing up in the figure.

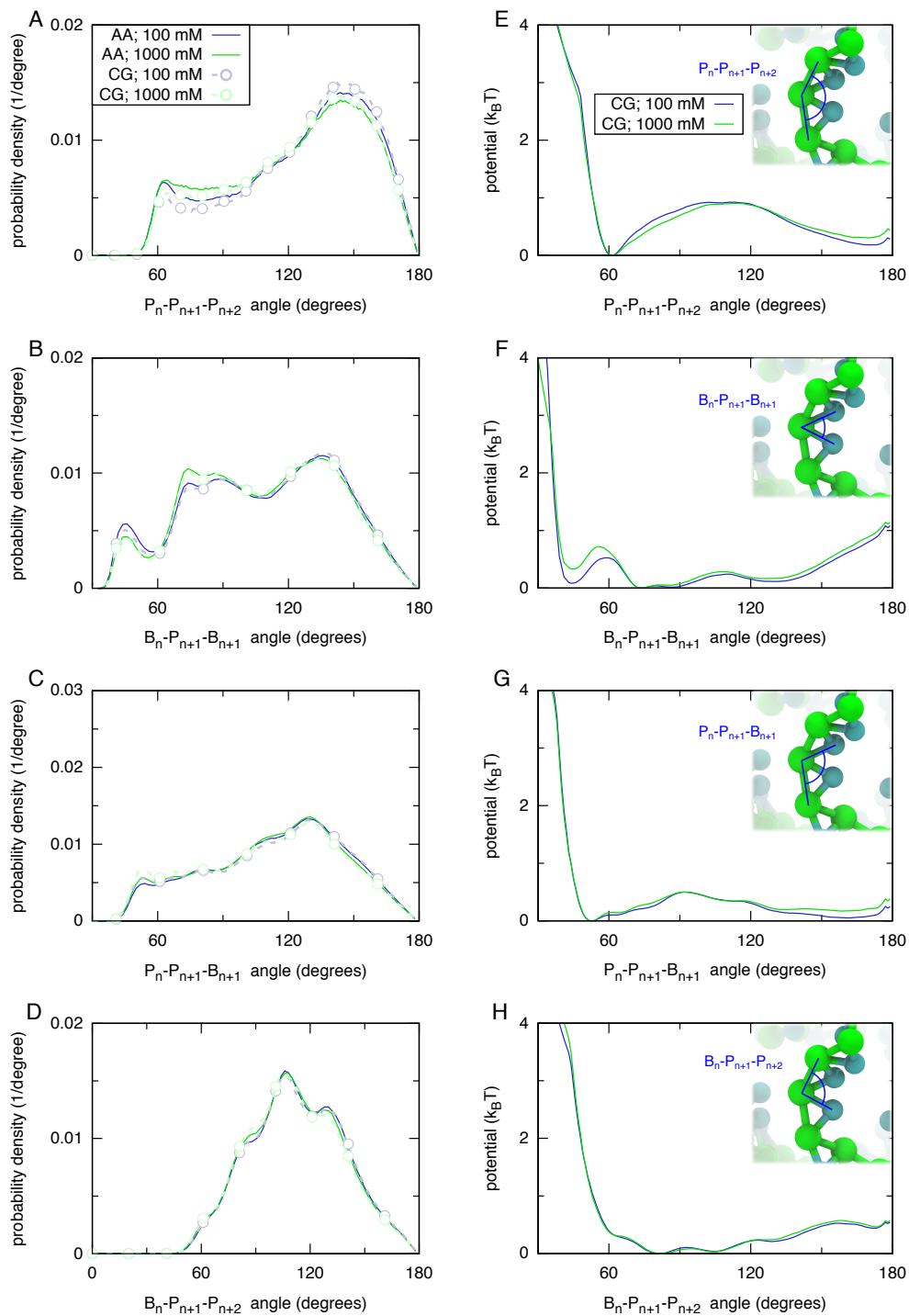


Figure S2: The distributions of angles (A-D) in all-atom and coarse-grained simulations of a dT₆₀ molecule and the corresponding CG potentials (E-H) at 1 degree resolution. The inset of each panel in (E-H) illustrates the angle characterized in that row of the figure. Colors and inset images are as in Figure S1.

in our two-beads-per-nucleotide CG model.

Figure S2A-D shows the distributions of the $P_n-P_{n+1}-P_{n+2}$, $B_n-P_{n+1}-B_{n+1}$, $P_n-P_{n+1}-B_{n+1}$, and $B_n-P_{n+1}-P_{n+2}$ angles considered in our model. The distributions are broad, spanning roughly 120° , and are poorly fit by single gaussians. The angle formed by three consecutive backbone beads ($P_n-P_{n+1}-P_{n+2}$) is likely to be around 140° regardless of the ion concentration, but with less likelihood at higher ion concentrations (presumably because of greater electrostatic screening allowing more “closed” conformations). Of the remaining distributions, only the angle between two consecutive bases ($B_n-P_{n+1}-B_{n+1}$) is significantly affected by the ion concentration. At 1000 mM, the likelihood of the $B_n-P_{n+1}-B_{n+1}$ angle to be between 40 and 60° is reduced, compared to the 100 mM case, but enhanced in the 60 to 90° interval. The $B_n-P_{n+1}-B_{n+1}$ angle appears to be anti-correlated with the backbone angle ($P_n-P_{n+1}-P_{n+2}$), Figure S3, suggesting that the ion concentration dependence of the former could derive from the ion concentration dependence of the latter.

Finally, the distributions of dihedral angles $P_n-P_{n+1}-P_{n+2}-P_{n+3}$, $B_n-P_n-P_{n+1}-B_{n+1}$, and $B_n-P_{n+1}-P_{n+2}-B_{n+2}$ are shown in Figure S4A-C. In 100 mM solvent, the backbone dihedral (Figure S4A) shows a weak preference for positive values over negative values, indicating a slight right-handed chirality along the 5'-to-3' direction. In 1000 mM solvent, this chirality nearly vanishes, and a preference for backbone dihedral angles around zero appears. The $B_n-P_n-P_{n+1}-B_{n+1}$ dihedral angle has peaks around 0 and 180° (Figure S4B), corresponding to the DNA conformations where neighboring bases are on the same side and on opposite sides of the DNA backbone. By contrast the $B_n-P_{n+1}-P_{n+2}-B_{n+2}$ dihedral angle has a single peak around zero (Figure S4C), indicating a preference for bases that are separated by a single base in between to lie on the same side of the DNA backbone.

The bonds, angles and dihedrals selected for our parameterization are fairly independent from one another (see Figure S3), suggesting that our all-atom system can be approximated well by a CG model that applies potentials to these degrees of freedom. Using an iterative refinement procedure described below, CG potentials were obtained for bonds (Figure S1D-F), angles (Figure S2E-H) and dihedral angles (Figure S4D-F).

Non-bonded interactions and potentials

The 1-3 excluded radial pair distribution functions (PDF) describing non-bounded interactions of two P, two B, and B and P type beads were obtained by first converting the all-atom MD trajectories into CG representations (CG mapping) and computing the unnor-

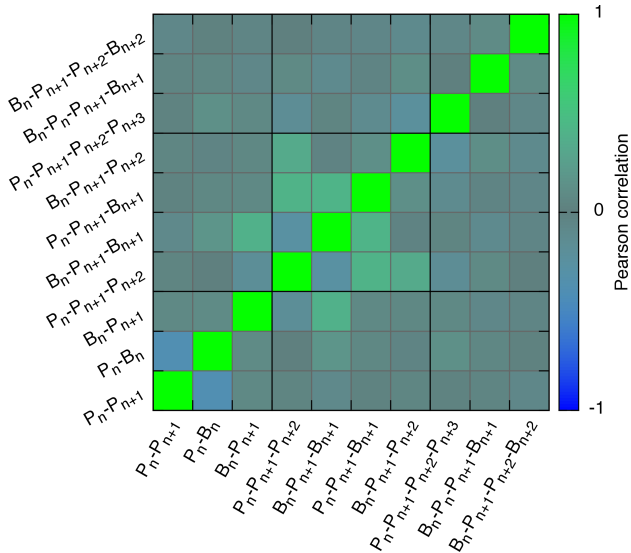


Figure S3: Pearson correlation for CG-mapped bonds, angles and dihedrals obtained from all-atom simulation. A value of 1 indicates perfect correlation, whereas a value of -1 indicates perfect anti-correlation.

malized PDF as $g_0(r) = \sum_{i,j} \frac{1}{4\pi r^2} \langle \delta(r_{i,j} - r) \rangle$. Here, 1-3 excluded means that the sum runs over only pairs of CG beads i, j that are at least two bonds apart. The angle brackets indicate averaging over MD trajectories. The normalized PDF was then produced using $g(r) = \frac{g_0(r)}{\int g_0(r') dr'}$. In practice, the PDF was calculated by binning the inter-bead distances at 0.05 \AA resolution.

As shown in Figure S5A-C, the PDF density for all bead types is nearly zero at small distances due to steric repulsion. The B-B bead distribution increases rapidly at around 4-\AA separation due to stacking interactions. Non-bonded CG potentials were obtained through iterative refinement so that the radial PDFs obtained in CG simulations accurately matched those obtained in all-atom simulation. The refinement process is described in detail below.

Iterative Boltzmann Inversion

Refinement of the CG potentials was performed against the distributions obtained from all-atom simulation following the iterative Boltzmann inversion (IBI) procedure. In IBI, a CG simulation yields a set of CG distributions. For a given pair of CG and target all-atom distributions, the CG potential is increased (decreased) at locations where the CG density is larger (smaller) than the all-atom density. This process is repeated until potentials are obtained that cause the CG distributions to converge to the target all-atom distributions.

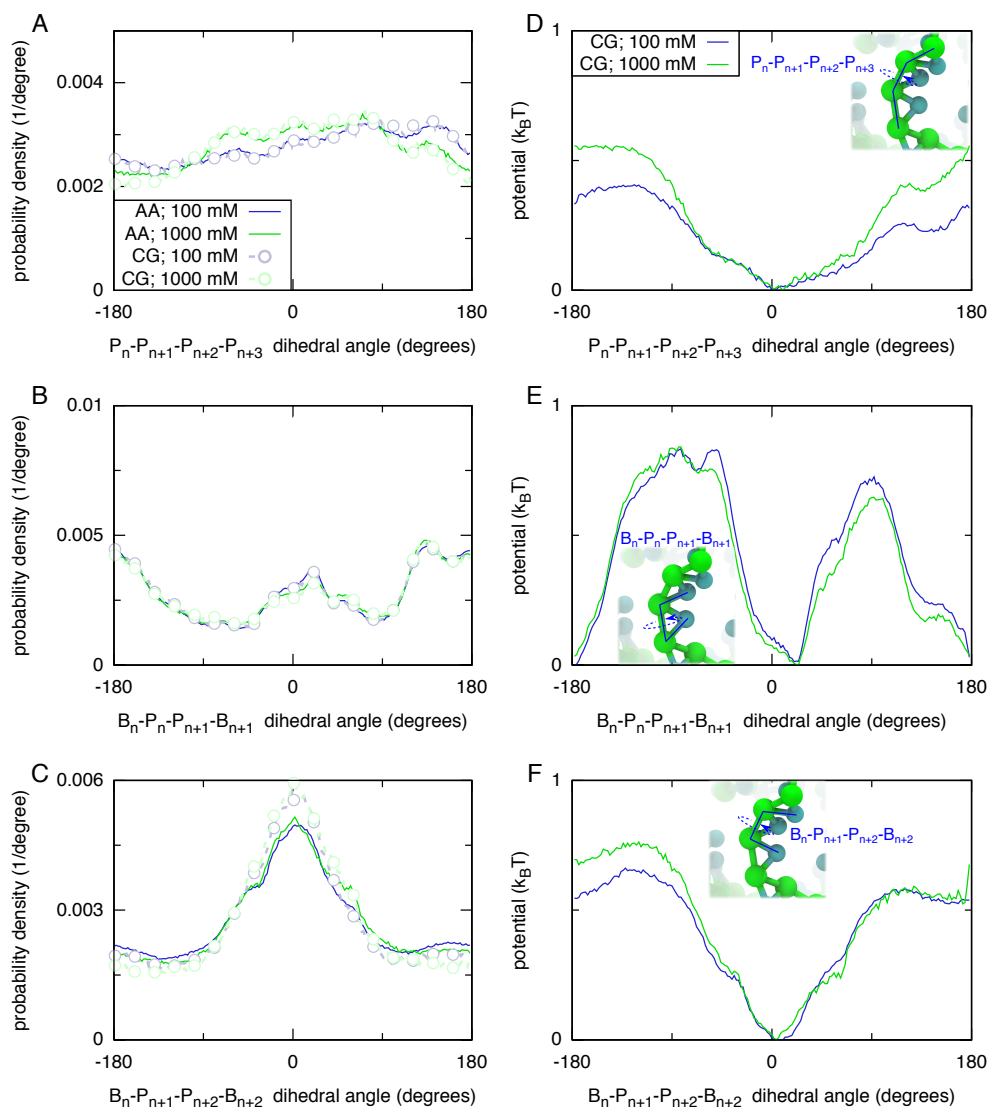


Figure S4: The distributions of dihedral angles (A-C) in all-atom and CG simulations of a dT₆₀ molecule and the corresponding CG potentials (D-F) at 2 degree resolution. The inset of each panel in (D-F) illustrates the dihedral angle characterized in that row of the figure. Colors and inset images are as in Figure S1.

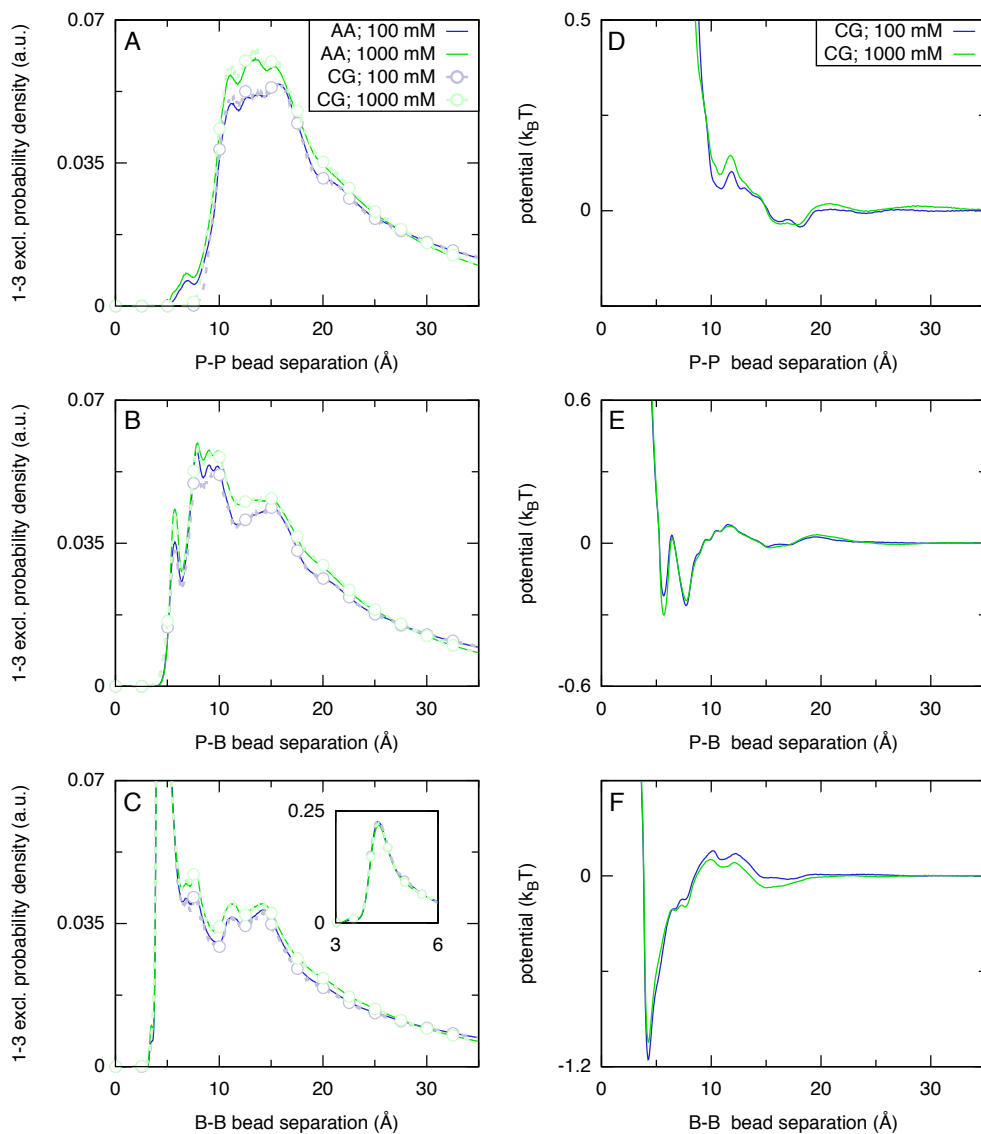


Figure S5: The normalized 1–3 excluded radial pair distribution functions (PDFs) (A–C) in all-atom and CG simulations of a dT_{60} molecule and the corresponding CG potentials (D–F) at 0.05 \AA resolution. The inset in (C) shows the peaks of the PDFs at close separation for B–B beads. Colors are as in Figure S1.

Refinement of bonded potentials

An initial guess for each CG potential was obtained through Boltzmann inversion of the corresponding all-atom (target) distribution followed by a triangular smoothing filter that was applied over 25, 11, and 5 points for bonds, angles and dihedrals, respectively, to mitigate the effects of noise.

The target distributions for bonds and angles had regions of zero values. Noise in the distributions bordering these empty regions can pose a significant impediment to the convergence of the refinement of the CG potentials. Therefore, regions where the density fell below 10^{-3} \AA^{-3} or $10^{-5} \text{ degree}^{-1}$ were replaced by a repulsive half-harmonic potential $u_{\text{wall}}(x) = U_0(x - x_{\text{wall}})^2 \times m_{\text{wall}}(x - x_{\text{wall}}) + U_{\text{wall}}$, where x_{wall} was the position where the density fell below the threshold, and the gradient and potential at x_{wall} were given by m_{wall} and U_{wall} , respectively. U_0 was $k_B T \text{ \AA}^{-2}$ for bonds and $\frac{k_B T}{180} \text{ degree}^{-2}$ for angles.

Each IBI iteration was performed as follows. Within each iteration, six CG simulations of dT₆₀ were performed in parallel to obtain six trajectories of approximately 1600 ns each (taking into account the factor of 80 speedup described below). Periodic boundary conditions were applied in the CG simulations according to the dimensions of the all-atom model. While keeping the non-bonded potentials fixed, bonded potentials were updated as $U_{n+1} = U_n - \alpha k_B T \log(\rho_{\text{CG}}(x)/\rho_{\text{target}}(x))$, using the bonded distributions $\rho_{\text{CG}}(x)$ extracted from the latest ensemble of simulations. The scaling factor α was set to 0.25 for angle and 0.5 for bond and dihedral potentials to ensure gradual convergence. The $\log(\rho_{\text{CG}}(x)/\rho_{\text{target}}(x))$ term was smoothed before it was added to the previous-generation potential U_n using the same smoothing filters as described above. The repulsive half-harmonic potentials at the boundaries of zero-density regions were updated. The final conformations of the dT₆₀ molecules from the ensemble of simulations were used as initial conformations for the next iteration. After thirty such iterations, the bonded potentials (Figures S1D-F, S2E-H, S4D-F) produced CG distributions (not depicted) in very close agreement with the all-atom distributions. The CG distributions shown in Figures S1, S2, S4 were taken from the final model, after refinement of both bonded and non-bonded potentials.

Refinement of non-bonded potentials against all-atom MD data

The initial non-bonded potentials were taken to be flat except in the regions where the normalized PDF was below 0.02 \AA^{-3} . In these regions, the potential was taken to be $u_{\text{wall}}(x) = U_0(x - x_{\text{wall}})^2 \times m_{\text{wall}}(x - x_{\text{wall}}) + U_{\text{wall}}$. This approach contrasts with the usual

IBI procedure, in which Boltzmann inversion of the radial distribution function provides the initial potential. We found, however, that using a flat initial potential was essential to ensure fast convergence of the iterative refinement. The difference in approach likely originates from the history of IBI that was commonly used as a tool to study polymer melts.¹⁵ Here, we adapt this approach to obtain potentials for a polymer in a dilute solution regime.

Iterative refinement of non-bonded potentials was performed exactly as in the case of bonded potentials, except that the bonded potentials were held fixed while the non-bonded potentials were varied. The (intra-chain) 1–3 excluded radial pair distribution functions (PDF), obtained for P–P, B–B, and B–P beads provided the density needed to update each non-bonded potential according to the IBI formula. Each update was smoothed by a triangular filter (10 points) before being added to the previous generation potential. Parameters of the harmonic wall that approximated steric repulsion at small distances were updated in each iteration.

For IBI refinement of the 100 mM model, all three non-bonded interactions were updated simultaneously. The scaling factor α was set to 0.3 for the first 44 iterations but was reduced to 0.05 for the final 24 iterations. Each iteration included 24 replicas; each replica was simulated for an equivalent of 1280 ns.

For the IBI refinement of the 1000 mM model, a slightly different procedure was adopted in an attempt to hasten convergence. With a value of 0.5 for the scaling factor, the B–B interaction was first refined for 14 iterations while all other potentials were held fixed. Then the B–P interaction was refined for 15 iterations while all other potentials (including B–B) were held fixed. Next the P–P interaction was refined for 5 iterations with the scaling factor set to 0.5, and then for 10 iterations with the scaling factor reduced to 0.1. Finally, all three non-bonded interactions were simultaneously refined for 120 iterations with the reduced scaling factor. Each iteration included 12 replicas; each replica was simulated for an equivalent of ~ 2500 ns.

At the end of these simulations, the non-bonded potentials (not depicted) provided CG PDFs (Figure S5A-C) that agreed well with the all-atom PDFs. Good agreement between all-atom and CG distributions of bonds, angles and dihedrals was maintained.

Refinement of non-bonded potentials against experimentally measured radius of gyration data

Throughout this study, the experimentally observed radius of gyration for a DNA molecule of a given length is taken to be the value given by the power law obtained by Sim et al. that best fits the ex-

perimental data.¹⁶ The radius of gyration of a dT₆₀ molecule simulated using the IBI-refined CG potentials was larger than the experimentally observed radius of gyration, $R_{\text{gyr,exp}}$.¹⁶ Therefore, additional refinement of the CG non-bonded P-P interaction was done for the 100 mM and 1000 mM models in 25 and 14 steps, respectively. During each step of refinement, 12 copies of a CG dT₆₀ molecule were each simulated in a cubic box 1000 Å on a side (preventing all interaction between periodic images) for at least an equivalent of ~ 1280 ns. At the end of the simulation, the average radius of gyration $R_{\text{gyr,CG}}$ was computed. The non-bonded P-P potential was adjusted by adding a scaled Yukawa potential $-k_B T \frac{R_{\text{gyr,CG}} - R_{\text{gyr,exp}}}{R_{\text{gyr,exp}}} \frac{1 \text{ nm}}{r} e^{-r/\lambda_{\text{DH}}}$, where r was the distance separating the beads and λ_{DH} was the Debye length at the appropriate ion concentration. The final potentials are shown in Figure S5D-F.

CG simulations of the force-extension dependence

A quantitative comparison of our CG model to the 3SPN.2 model was done by measuring the extension of a dT₂₀₀ molecule under external force. Extension of a 200-nt base-average model of DNA was simulated to test the oxDNA model. The simulations of 3SPN.2 DNA were performed using LAMMPS.¹⁷ The simulations of oxDNA were performed using the oxDNA software.¹⁸ For each data point reported in Figures 2,3 of the main text, one simulation was performed. Forces of the same magnitude but opposite directions were applied to the ends of the DNA molecule, stretching the latter. Projection of the end-to-end distance on the axis defined by the direction of the applied forces was recorded. The average extension was obtained by discarding the initial 50 ns of the trajectory required to reach a steady state and averaging over the remaining frames of the trajectory, which typically covered at least 1,000 ns. For most data points shown in Figures 2 and 3, the error bars are smaller than the symbols.

The time scale of CG simulations

Coarse-graining, in general, involves smoothing out many degrees of freedom. As a result, processes tend to occur faster in a CG simulation than prescribed by its nominal time steps.¹⁹ In our particular model, the effect of solvent is represented solely through the Langevin thermostat that adds independent random forces and viscous drag forces to each particle of the model. Hence, the polymers described by our model exhibit Rouse-like dynamics.²⁰ For example, the diffusion coefficient of a molecule scales as $1/N$, where N is the number of nucleotides. Experimentally, the dif-

fusion of single-stranded DNA molecules is observed to scale as $1/\sqrt{N}$,²¹ consistent with the Rouse-Zimm polymer model, which incorporates hydrodynamic interactions between beads.²² Unfortunately, hydrodynamic interactions are long-range, and rather expensive to calculate, even approximately.²³ Support for calculating hydrodynamic interactions is lacking in many popular molecular dynamics codes. Accordingly, hydrodynamic interactions are not present in our model, and a chain-length-dependent deviation from experimental timescales can be expected.

Many of the simulations in this study were performed using a dT₆₀ molecule. The most important timescales with respect to sampling are the internal dynamics of the molecule. Experimentally, the timescale of end-to-end collisions for a 20 nt DNA fragment was measured to be 800 ns and was found to scale as $N^{3.5}$ with the length of the fragment.²⁴ From our simulations, the timescale of end-to-end collision for a dT₂₀ molecule was estimated to be range between 2 and 20 ns, depending on the definition of what constitutes a collision event (the end-to-end distance range of 15–25 Å). Furthermore, we found the collision timescale to scale roughly as $N^{2.8}$ for molecules ranging from 8 to 100 nt. Thus, for a dT₆₀ molecule, the end-to-end collision dynamics should be enhanced by a factor of roughly 80. We take this factor into account when we report the CG simulation times.

Preparation of a DNA construct for fleezers measurement

The DNA construct was made from two DNA oligos 5′-5Phos/GGG CGG CGA CCT T /iAmMC6T/T TTT TTT TTT TTT GCC TCG CTG CCG TCG CCA and 5′-TGG CGA CGG CAG CGA GGC /3Cy5Sp/ (IDT DNA). The first oligo was labeled with Cy3-NHS (GE Healthcare) according to Roy et al.²⁵ The two oligos were annealed by mixing at 1:1 molar ratio of 10 μM in T50 buffer (10 mM Tris-HCl pH 8, 50 mM NaCl) and heating to 90° C for 5 min followed by slow cooling over 4 hours. After that, the DNA construct was annealed to λ-phage DNA (NEB) and an oligonucleotide containing digoxigenin. First, we added 1 μl of 5 M NaCl and 1 μl of 100 mM MgCl₂ electrolytes to 40 μl λ-phage DNA stock of ~ 16 nM (NEB) in an Eppendorf tube. The mixture was heated to 80° C for 10 min, and then placed on ice for 5 min. The DNA constructs were added to a final concentration of 8 nM and BSA was added to a final concentration of 0.1 mg/ml. The tube was covered in foil and the mixture was incubated in the dark with rotation at room temperature for 2-3 hours. DIG oligo 5′-AGG TCG CCG CCC TTT/digoxigenin/ (IDT DNA) was added to a final concentration of 0.2 μM and then incubated with rotation at room temperature for 1-2

hours. This sample was stored at -20° C until assembly on a microscope slide for single-molecule data acquisition.

Stretching dT₁₄ using fleezers

The DNA sample was assembled on a glass surface coated with polyethyleneglycol (mixture of mPEG-SVA and Biotin-PEG-SVA, Laysan Bio) according to Roy et al. Before adding the DNA sample, the surface was incubated with neutravidin at 0.25 mg/ml for 5 minutes and then blocking buffer (10 mM Tris-HCl pH 8, 50 mM NaCl, 1 mg/ml BSA (New England Biolabs), 1 mg/ml tRNA (Ambion)) for 1 hour. The DNA construct was then incubated on the surface at the concentration of 20 pM in T50 buffer (10 mM Tris-HCl pH 8, 50 mM NaCl) for 10 min. Next, anti-dioxigen-coated 1 μ m polystyrene beads (Polysciences) diluted in T50 buffer were added to the imaging chamber for about 30 minutes to allow attachment of beads to the free end of each tether. Finally, the imaging buffer (20 mM Tris-HCl pH 8, 0.5 mg/ml BSA (NEB), 0.1% v/v Tween-20 (Sigma), 0.5% w/v D-Glucose (Sigma), 165 U/ml glucose oxidase (Sigma), 2170 U/ml catalase (Roche), 3 mM Trolox (Sigma)) and NaCl electrolyte of 10 mM or 100 mM or 1 M was added for data acquisition. Single-molecule data acquisition was performed according to Hohng et al.²⁶ The full description of the setup can be found in our recent review Zhou et al.²⁷ The DNA stretching experiment was performed by moving the stage in steps at the average loading rate of 455 nm/s. The confocal excitation was scanned following the stage movement. Fluorescence emission was detected for 20 ms after each movement step of the stage. All experiments were carried at room temperature (22° C).

Preliminary dsDNA model

A toy model of double-stranded DNA was constructed from the CG ssDNA model by adding a set of harmonic potentials between beads involved in base-pairing. Specifically, restrained bonds included the base pairing term P_i-P_j ($r_0 = 7.8 \text{ \AA}$; $k = 10 \frac{\text{kcal}}{\text{mol \AA}^2}$), and cross-stacking terms P_i-P_{j-1} ($r_0 = 8.1 \text{ \AA}$) and P_i-P_{j+1} ($r_0 = 8.0 \text{ \AA}$) with $k = a \frac{\text{kcal}}{\text{mol \AA}^2}$, where r_0 is the rest length, k is the spring constant, a is the scaling factor used to tune the persistence length of the model, j is taken to be the pair of nucleotide i , and the subscripts increase along the 5'-to-3' direction. Restrained angles included backbone restraints $P_i-P_{i+1}-P_{i+2}$ and $P_j-P_{j+1}-P_{j+2}$ ($\theta_0 = 150^{\circ}$), additional intra-strand restraints $P_i-P_{i+1}-B_{i+1}$ and $P_j-P_{j+1}-B_{j+1}$ ($\theta_0 = 87^{\circ}$), and inter-strand restraints $P_i-B_i-B_j$ and $P_j-B_j-B_i$ ($\theta_0 = 162^{\circ}$), where θ_0 is the rest angle of the restraint and all angle restraints employed

the spring constant $k = 90a \frac{\text{kcal}}{\text{mol degree}^2}$. The rest lengths of all potentials were obtained from canonical poly(dT)·poly(dA). By changing the scaling factor a , the double-stranded DNA could be made stiffer or more flexible. Using a scaling factor of $a = 1$ was found to produce dsDNA with approximately the correct persistence length.

References

- [1] Phillips, J. C.; Braun, R.; Wang, W.; Gumbart, J.; Tajkhorshid, E.; Villa, E.; Chipot, C.; Skeel, R. D.; Kale, L.; Schulten, K. *J. Comput. Chem.* **2005**, *26*, 1781–1802.
- [2] Hart, K.; Foloppe, N.; Baker, C. M.; Denning, E. J.; Nilsson, L.; MacKerell, A. D. *J. Chem. Theory Comput.* **2012**, *8*, 348–362.
- [3] Denning, E. J.; Priyakumar, U. D.; Nilsson, L.; Mackerell, A. D. *J. Comput. Chem.* **2011**, *32*, 1929–1943.
- [4] MacKerell Jr., A. D.; Banavali, N. K. *J. Comput. Chem.* **2000**, *21*, 105–120.
- [5] Foloppe, N.; MacKerrell Jr., A. D. *J. Comput. Chem.* **2000**, *21*, 86–104.
- [6] Jorgensen, W. L.; Chandrasekhar, J.; Madura, J. D.; Impey, R. W.; Klein, M. L. *J. Chem. Phys.* **1983**, *79*, 926–935.
- [7] Beglov, D.; Roux, B. *J. Chem. Phys.* **1994**, *100*, 9050–9063.
- [8] Yoo, J.; Aksimentiev, A. *J. Phys. Chem. Lett.* **2012**, *3*, 45–50.
- [9] Essmann, U.; Perera, L.; Berkowitz, M. L.; Darden, T.; Lee, H.; Pedersen, L. G. *J. Chem. Phys.* **1995**, *103*, 8577–8593.
- [10] Batcho, P. F.; Case, D. A.; Schlick, T. *J. Chem. Phys.* **2001**, *115*, 4003–4018.
- [11] Miyamoto, S.; Kollman, P. A. *J. Comput. Chem.* **1992**, *13*, 952–962.
- [12] Andersen, H. *J. Comp. Phys.* **1983**, *52*, 24–34.
- [13] Brünger, A. T. X-PLOR, Version 3.1: A System for X-ray Crystallography and NMR. The Howard Hughes Medical Institute and Department of Molecular Biophysics and Biochemistry, Yale University, 1992.
- [14] Martyna, G. J.; Tobias, D. J.; Klein, M. L. *J. Chem. Phys.* **1994**, *101*, 4177–4189.
- [15] Reith, D.; Pütz, M.; Müller-Plathe, F. *J. Comput. Chem.* **2003**, *24*, 1624–1636.

- [16] Sim, A.; Lipfert, J.; Herschlag, D.; Doniach, S. *Phys. Rev. E* **2012**, *86*, 1–5.
- [17] Plimpton, S. *J. Comp. Phys.* **1995**, *117*, 1–19.
- [18] Ouldridge, T. E.; Louis, A. A.; Doye, J. P. K. *J. Chem. Phys.* **2011**, *134*, 085101.
- [19] Zwanzig, R. *Proc. Natl. Acad. Sci. U.S.A.* **1988**, *85*, 2029–2030.
- [20] Rouse, P. E. *J. Chem. Phys.* **1953**, *21*, 1272–1280.
- [21] Nkodo, A. E.; Garnier, J. M.; Tinland, B.; Ren, H.; Desruissaux, C.; McCormick, L. C.; Drouin, G.; Slater, G. W. *Electrophoresis* **2001**, *22*, 2424.
- [22] Zimm, B. H. *J. Chem. Phys.* **1956**, *24*, 269.
- [23] Pham, T. T.; Schiller, U. D.; Prakash, J. R.; Dünweg, B. *J. Chem. Phys.* **2009**, *131*, 164114.
- [24] Uzawa, T.; Isoshima, T.; Ito, Y.; Ishimori, K.; Makarov, D. E.; Plaxco, K. W. *Biophys. J.* **2013**, *104*, 2485–2492.
- [25] Roy, R.; Hohng, S.; Ha, T. *Nature Meth.* **2008**, *5*, 507–516.
- [26] Hohng, S.; Zhou, R.; Nahas, M. K.; Yu, J.; Schulten, K.; Lilley, D. M. J.; Ha, T. *Science* **2007**, *318*, 279–83.
- [27] Zhou, R.; Schlierf, M.; Ha, T. *Methods in Enzymology*, 1st ed.; Elsevier Inc., 2010; Vol. 475; Chapter 6, pp 405–426.